Optimisation of image reconstruction for phase-contrast x-ray Talbot–Lau imaging with regard to mechanical robustness

M Seifert[1], S Kaeppler[2], C Hauke[1], F Horn[1], G Pelzer[1], J Rieger[1], T Michel[1], C Riess[2] and G Anton[1]

[1] ECAP—Novel Detectors/Medical Physics, Friedrich-Alexander-University Erlangen-Nuremberg, Erwin-Rommel-Strasse 1, Erlangen, Germany
[2] Pattern Recognition Lab, Friedrich-Alexander-University Erlangen-Nuremberg, Martensstrasse 3, Erlangen, Germany

E-mail: maria.seifert@fau.de

Abstract

X-ray grating-based phase-contrast imaging opens new opportunities, inter alia, in medical imaging and non-destructive testing. Because, information about the attenuation properties and about the refractive properties of an object are gained simultaneously.

Talbot–Lau imaging requires the knowledge of a reference or free-field image. The long-term stability of a Talbot–Lau interferometer is related to the time span of the validity of a measured reference image. It would be desirable to keep the validity of the reference image for a day or longer to improve feasibility of Talbot–Lau imaging.

However, for example thermal and other long-term external influences result in drifting effects of the phase images. Therefore, phases are shifting over time and the reference image is not valid for long-term measurements. Thus, artifacts occur in differential phase-contrast images. We developed an algorithm to determine the differential phase-contrast image with the help of just one calibration image, which is valid for a long time-period. With the help of this algorithm, called phase-plane-fit method, it is possible to save measurement-time, as it is not necessary to take a reference image for each measurement.

Additionally, transferring the interferometer technique from laboratory setups to conventional imaging systems the necessary rigidity of the system is difficult to achieve. Therefore, short-term effects like vibrations or distortions of the system lead to imperfections within the phase-stepping procedure. Consequently, artifacts occur in all three image modalities (differential phase-contrast image, attenuation image and dark-field image) of Talbot–Lau imaging. This is a problem with regard to the intended use of phase-contrast imaging for

example in clinical routine or non-destructive testing. In this publication an algorithm of Vargas *et al* is applied and complemented to correct inaccurate phase-step positions with the help of a principal component analysis (PCA). Thus, it is possible to calculate the artifact free images. Subsequently, the whole algorithm is called PCA minimization algorithm.

Keywords: x-ray imaging, phase-contrast, Talbot–Lau, image reconstruction, PCA, reference phase, robustness

(Some figures may appear in colour only in the online journal)

1. Introduction

In conventional x-ray imaging the attenuation image of an object is acquired, which implies a good bone-tissue contrast with regard to medical imaging. Various techniques have been applied to get further information about an object in the beam-path. These techniques can be divided in five main categories (Diemoz *et al* 2012): the interferometric methods using crystals (Momose *et al* 1996), the propagation-based methods (Snigirev *et al* 1995, Wilkins *et al* 1996), the analyzer-based methods (Foerster *et al* 1980, Chapman *et al* 1997, Bravin 2003), the grating interferometric methods (David *et al* 2002, Weitkamp *et al* 2005, Pfeiffer *et al* 2006a) and the grating non-interferometric methods (Olivo *et al* 2001, Olivo and Speller 2007, Olivo *et al* 2011). In this work the grating based interferometric Talbot–Lau method is applied.

Using a Talbot–Lau interferometer (Talbot 1836, Lau 1948, Jahns and Lohmann 1979, Bartelt and Jahns 1979, Patorski *et al* 1983, Clauser and Reinsch 1992, Suleski 1997, Pfeiffer *et al* 2006a) further information about the phase-shift and the scattering properties of the object can be obtained simultaneously (Li *et al* 2014). This allows to gain a better soft tissue contrast and therefore prices this technique as a very promising imaging modality in medical imaging (Momose *et al* 1996, Fitzgerald 2000, Pfeiffer *et al* 2006a, Stampanoni *et al* 2011, Michel *et al* 2013, Bech *et al* 2013, Li *et al* 2014) and non-destructive testing (Pfeiffer *et al* 2006a). It is for example possible to show up micro calcifications in mammography (Stampanoni *et al* 2011, Michel *et al* 2013) and to depict lung tissue (Bech *et al* 2013). This might give the opportunity to diagnose breast tumors (Stampanoni *et al* 2011, Michel *et al* 2013) and lung diseases like emphysema (Bech *et al* 2013) earlier. However, the x-ray phase-contrast setup is sensitive to vibrations, thermal effects and mechanical inaccuracies of the grating positions (Tapfer *et al* 2012, Koehler *et al* 2015). These impacts can be differentiated on three time scales:

  (i) very short-term is the exposure time at a single phase-step position, in the terms of milliseconds,
 (ii) short-term is the time needed to acquire a phase-stepping curve, in the terms of seconds and
(iii) long-term is more than that, in the terms of minutes up to hours.

Talbot–Lau imaging requires the knowledge of a reference or free-field phase image to characterize the setup. For measuring the reference image no object should be in the beam-path. The long-term stability of a Talbot–Lau interferometer is thus related to the time span of the validity of a measured reference image. Due to the relatively small size of available gratings large object have to be scanned by a multiple of partial images. The time needed to image for instance a human knee may lie of the order of hours. Accordingly, it would be desirable to

keep the validity of a reference image for such time scales. It is expected that with large gratings the acquisition time will go down to seconds. But for clinical routine it would be desirable that one reference image is valid for a long term period like a day or a week. Especially e.g. in fluoroscopy the short validity of a reference image poses many problems as there is not enough time to take the required amount of reference images. With the help of the proposed image reconstruction algorithm, subsequently called phase-plane-fit method (PPF), it is possible to reconstruct a phase-contrast image using just one reference image. This is better compatible with clinical workflow as the image acquisition procedure becomes the same as in conventional x-ray imaging.

The phase-contrast image is usually reconstructed by Fourier-analysis (FFT) (Engelhardt *et al* 2008) or least square fitting routine of the phase-stepping dataset. For both methods it is necessary to know the exact phase-step positions. These are well known for the interferometer mounted on a laboratory optical table. Transferring the technique to a conventional imaging system, vibrations and distortions during the acquisition procedure lead to artifacts in the obtained images if the conventional reconstruction methods are applied. To retrieve the phase-information from unknown phase-step positions Vargas *et al* (2011) proposed an algorithm based on principal component analysis (PCA) for optical light interferometry. This method was recently transferred to x-ray phase-imaging by Pelzer *et al* (2015). So far, only the reconstruction of the differential phase-contrast image was achieved with the help of the PCA algorithm. In this work an advanced algorithm of Vargas *et al* (2013) is used to also obtain the accurate phase-step positions and—combined with standard sine fit reconstruction—to obtain the attenuation and dark-field images, as well.

2. Materials and methods

2.1. Talbot–Lau interferometry

To measure the effect of objects on the phase, the amplitude and the offset of the spatially coherent wavefront, a Talbot–Lau interferometer is used (Lohmann and Silva 1971, Momose *et al* 2003, Pfeiffer *et al* 2006b) (figure 1).

As it is not possible to measure the absolute phase of a wavefront, the refraction angle of a spatially coherent wavefront is analyzed. The refraction of the wavefront leads to a phase-shift of the wavefront in front of the detector. As only the effects of the object on the wavefront should be analyzed, a phase-map of the free-field is taken, recently called reference phase.

The Talbot-effect descibes the formation of self-images of the phase grating G_1 in so called Talbot-distances behind the grating if it is illuminated by a spatially and temporally coherent wavefront. An object between the x-ray source and the grating G_1 refracts the coherent wavefront (Talbot 1836, Suleski 1997). The refraction is caused by a phase-shift which results from the speedup of the wavefront passing the object. This is specific for each material and is described by its complex index of refraction $n = 1 - \delta + i\beta$, where β describes the attenuation of x-rays and δ the phase-shift within the material (Fitzgerald 2000). Thus, the deflection of the wavefront is observed as a local shift of the Talbot-intensity pattern behind G_1 perpendicular to the direction of propagation. As the detector pixels are usually much larger than the period of the intensity pattern, an analyzer grating G_2 has to be placed in a fractional Talbot distance behind G_1, which serves as an absorption mask. G_2 is moved in front of the detector perpendicular to the grating bars by fractions of its period. After each movement an image is acquired. The intensity measured in each pixel of the detector depends on the position of G_2 compared to the intensity pattern. Thereby, the pattern is sampled (Weitkamp *et al* 2005). Subsequently the positions of G_2 are called phase-step positions.
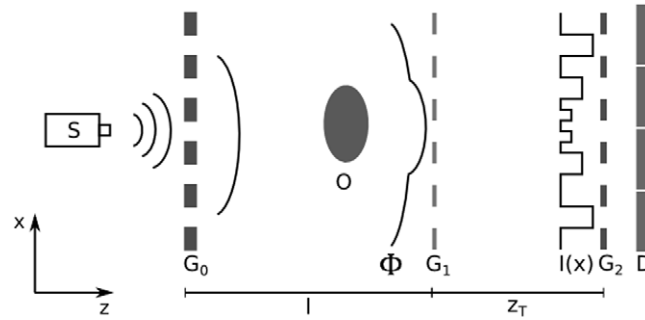
Figure 1. Setup of a Talbot–Lau interferometer. The object *O* deforms the wave front emitted by the source *S*. Because of the Lau-effect (due to the gratings G_0 and G_1) a periodic intensity pattern can be observed in a Talbot distance behind G_1. The period of the intensity pattern is small, compared to the size of the detector pixel. To be able to measure the pattern a phase-stepping is performed with a third grating G_2. It is used to sample the intensity pattern and has to be placed in the Talbot distance z_T downstream of G_1. *l* has to be determined applying the intercept theorem.

With the help of this stepping method for each pixel of the detector the information about the phase-shift ϕ, the amplitude *A* and the mean intensity I_0 of the intensity pattern is known. The visibility *V* is defined as $V = \frac{A}{I}$. The variable *N* describes the amount of phase-steps of G_2 and *p* the number of periods of the intensity pattern which are sampled. The intensity at the nth phase-step position can be described by Weber *et al* (2011) $I(n) = I_0 \cdot \left(1 + V \cdot \sin\left(\frac{2\pi np}{N} + \phi\right)\right)$ with $n \in 0, ..., N-1$. With knowledge of the equidistant phase-step positions $\frac{2\pi np}{N}$, a least square fitting algorithm of a sinusoidal-curve can be performed. To get the accurate sine function, the phase-step positions have to be known precisely. Otherwise the calculated parameters would be slightly wrong. That would lead to image artifacts.

The three imaging modalities can be calculated for each pixel using the fitted parameters I_0, *V* and ϕ as follows

$$\text{attenuation image:} \quad T = -\ln\left(\frac{I_{0,\text{obj}}}{I_{0,\text{ref}}}\right) \tag{1}$$

$$\text{differential phase-contrast image:} \quad d_\phi = (\phi_{\text{obj}} - \phi_{\text{ref}})(\text{mod}\,2\pi) \tag{2}$$

$$\text{dark-field image:} \quad D = -\ln\left(\frac{V_{\text{obj}}}{V_{\text{ref}}}\right) \tag{3}$$

Using a polychromatic x-ray source with a large focus, a third grating G_0 which is placed just behind the focus is required. This creates mutually independent slit sources whereas each of them behaves like a single coherent source (Pfeiffer *et al* 2006a, David *et al* 2006, Weitkamp *et al* 2006).

2.2. Setup

The image data shown in this publication are acquired in a setup for x-ray grating-based Talbot–Lau imaging described in the following. A phase-shift of $\frac{\pi}{2}$ caused by the phase grating

Table 1. High-energy setup: distances between the components.

Source grating (G_0)—sample	59.3 cm
Sample—phase grating (G_1)	41.1 cm
Phase grating (G_1)—analyzer grating (G_2)	41.0 cm

Table 2. High-energy setup: properties of the gratings.

	G0	G1	G2
Material	Au	Au	Au
Period (μm)	11.54	3.39	4.8
Height of bars (μm)	290	6.37	180
Duty cycle	0.5	0.5	0.5

G_1 can be achieved at the designed energy of 62.5 kV. It is possible to use acceleration voltages between 50 kV and 125 kV without lowering visibility to much. In the setup a Siemens MEGALIX Cat Plus 125/40/90-125GW is used as x-ray source. The detector is a PerkinElmer DEXELA 1512 with 75 μm pixelpitch. Tables 1 and 2 show further properties of the setup.

2.3. Specimen

An image of a complete human hand (*ex vivo*) is shown in this publication. It consists of 70 partial images or tiles due to the limited grating size which results in a field of view of about 1.4 cm $\times$ 3.2 cm. The acquisition time is calculated for each tile individually depending on the absorption property of the object in the beam path. The tube voltage has been 75 kV and the tube current 15 mA. The dose applied in the different tiles was between 0.17 mGy and 0.49 mGy in air kerma. The specimen are provided by Paulsen, medical director of the anatomical institute II of Friedrich-Alexander University Erlangen-Nuremberg.

2.4. Long-term drift effects

In x-ray phase-contrast imaging the incident wave is diffracted by the object in the beam path. This diffraction leads to a lateral shift of the Talbot fringes in the plane of the analyzer grating. The size of the shift depends on the diffraction index of the object. It can be measured as the phase-shift $\phi(x, y)$ of the incident wave downstream of the phase grating G_1 in each detector pixel (x, y). Measurements show that this phase-shift is time-dependent $\phi(x, y, t)$. This time dependency can be due to thermal effects in the imaging system. Figure 2 shows the time dependency of a phase-map (reference phase) $\phi(x, y)$.

To extract the information of the phase $\phi_{obj}(x, y, t_{obj})$ with the object in place, it is necessary to substract the phase of the free-field, the reference phase $\phi_{ref}(x, y, t_{ref})$. Due to the time dependency of the phase it would be advantageous to measure the object phase $\phi_{obj}(x, y, t_{obj})$ and the reference phase $\phi_{ref}(x, y, t_{ref})$ rightly consecutively, with $\Delta t = t_{obj} - t_{ref}$ as small as possible. In the (medical) workflow it is often not possible to perform a measurement under these conditions. There, the patient needs some time to be positioned or there is not enough time to take a reference image for each patient. Also in non-destructive testing it may not be possible to take reference images as often as it would be necessary to achieve artifact free images.

Because of the limited field of view due to the size of our analyzer grating it is necessary to tile the image in many partial images. Figure 3 shows the result of a reconstruction of a differential phase-contrast image of a human hand (*ex vivo*) using just one reference phase image
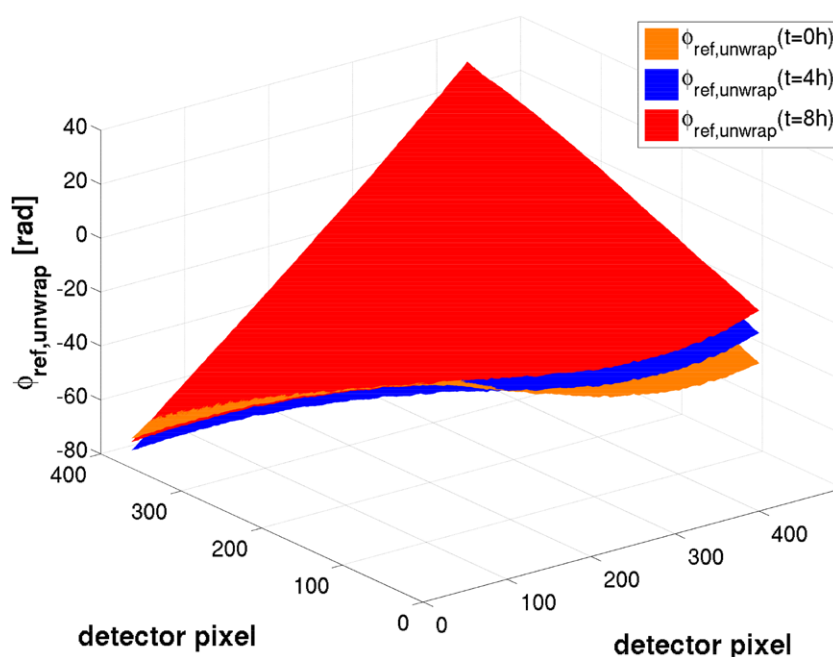
Figure 2. Reference phase images taken at three different times: plot of unwrapped reference phase images: $\phi_{\text{ref, unwrap}}(t = 0\ \text{h})$ (orange), $\phi_{\text{ref, unwrap}}(t = 4\ \text{h})$ (blue) and $\phi_{\text{ref, unwrap}}(t = 8\ \text{h})$ (red).
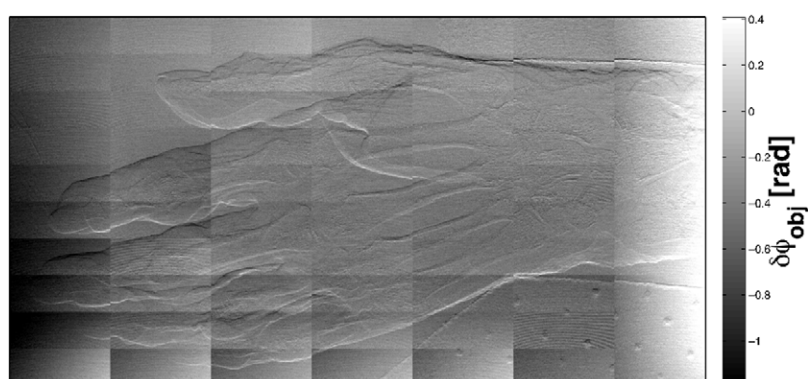

Figure 3. Differential phase-contrast image of a human hand, reconstructed using just one reference phase image, taken at the beginning of the measurement. The whole measurement took about 45 min. Structural information of the hand is superimposed by artifacts, caused by drift of the phase.

taken at the beginning of the measurement. Structural information of the object is superimposed by artifacts which are caused by phase drifting effects.

In figure 4 a reference image taken for the image of the human hand is shown. Due to grating imperfections and not perfectly aligned gratings the reference phases vary from pixel to pixel within the interval $[0, 2\pi]$. To smoothen the reference phase image an unwrapping algorithm is performed (figure 5). After performing the unwrapping algorithm the phase-map can be modeled
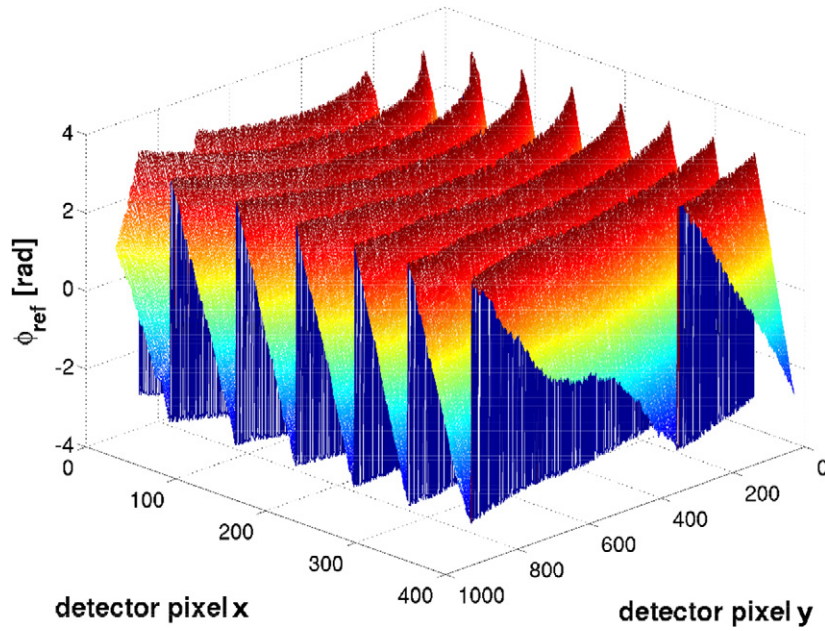
Figure 4. Reference phase image ϕ_{ref} in the FoV.

by a polynomial. Thus, a 2D 5th degree polynomial is fitted in the measured and unwrapped phase image (figure 6). The degree of the polynomial has been found empirically. It is the best compromise between the computing time on the one hand and the goodness of fit on the other hand.

After performing the fit algorithm the residuals between the measured phase and the fit polynomial are calculated, using $\phi_{\text{res}}(x, y, t) = \phi_{\text{unwrap}}(x, y, t) - \phi_{\text{fit}}(x, y, t)$.

Figures 7–9 show that the time-dependence of the residuals $\phi_{\text{res}}(x, y, t)$ is small with a root mean square of $\langle \sqrt{(\phi_{\text{res}}(x, y, t_1) - \phi_{\text{res}}(x, y, t_2))^2} \rangle_{x,y} = 0.0036$ rad: $\phi_{\text{res}}(x, y, t) \simeq \phi_{\text{res}}(x, y)$. This can be explained by the fact that the residuals result from inhomogeneities of the gratings. These inhomogeneities are time-independent. Additionally, it is presumed that a polynomial, fitted in the phase image, measured with an object in the beam is almost the same as a polynomial, fitted in the reference phase, measured at the same time. It can be assumed that the influences of the object on the phase do not affect the general form of the polynomial as long as the object does not shift the phase of the complete FoV in just one direction. The information about the object is predominantly contained in the residuals between the measured object phase and the polynomial fit $\phi_{\text{res, obj}}(x, y, t) = \phi_{\text{obj, unwrap}}(x, y, t) - \phi_{\text{obj, fit}}(x, y, t)$. That means that the residuals $\phi_{\text{res, obj}}(x, y, t)$ include the object information and the information about the inhomogeneities of the setup. Since the information about the inhomogeneity of the setup is time-independent, the object information can be calculated by subtracting the residuals of a reference phase measurement taken at any time: $\delta\phi_{\text{obj}}(x, y) = \phi_{\text{res, obj}}(x, y) - \phi_{\text{res, ref}}(x, y)$. Equation (4) summarizes the whole procedure.

$$\delta\phi_{\text{obj}}(x, y) = \phi_{\text{obj, unwrap}}(x, y, t) - \phi_{\text{obj, fit}}(x, y, t) - \phi_{\text{res, ref}}(x, y) \tag{4}$$

This method of calculating the object information without taking continuously new reference images will be referred to as plane-phase-fit method (PPF).
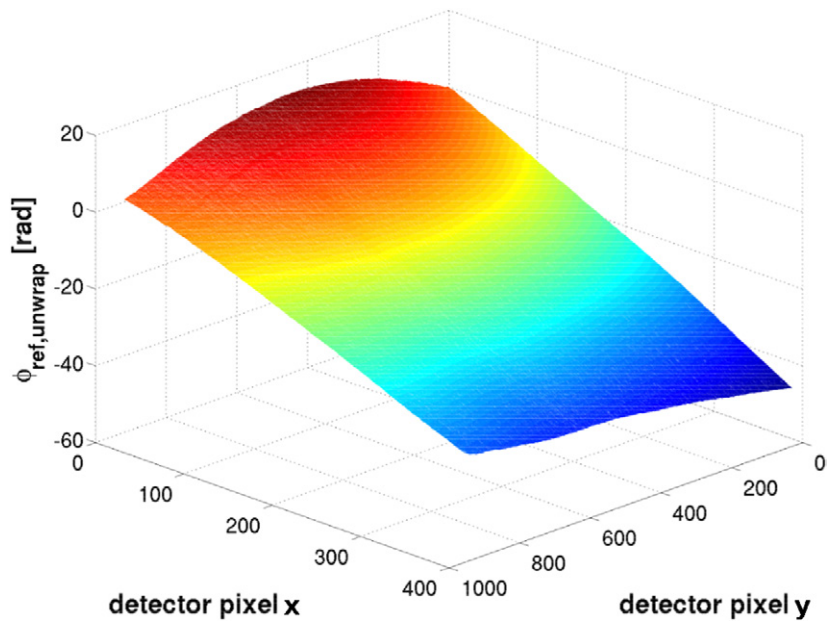
Figure 5. Reference phase image after applying an unwrapping algorithm ($\phi_{\text{ref, unwrap}}$).
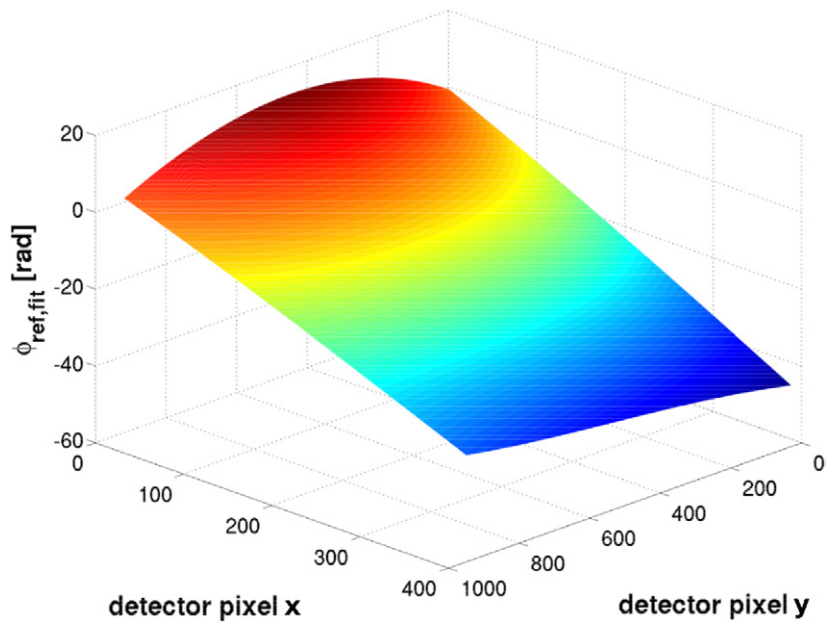

Figure 6. Fit of a 2D polynomial of 5th degree in the unwrapped reference phase image ($\phi_{\text{ref, fit}}$).

Applying the PPF, slow temporal changes of the object phase might be absorbed by the fitted polynomial. Since the information described by the polynomial is not considered for calculating the object information, large spacial frequency properties of the object are not
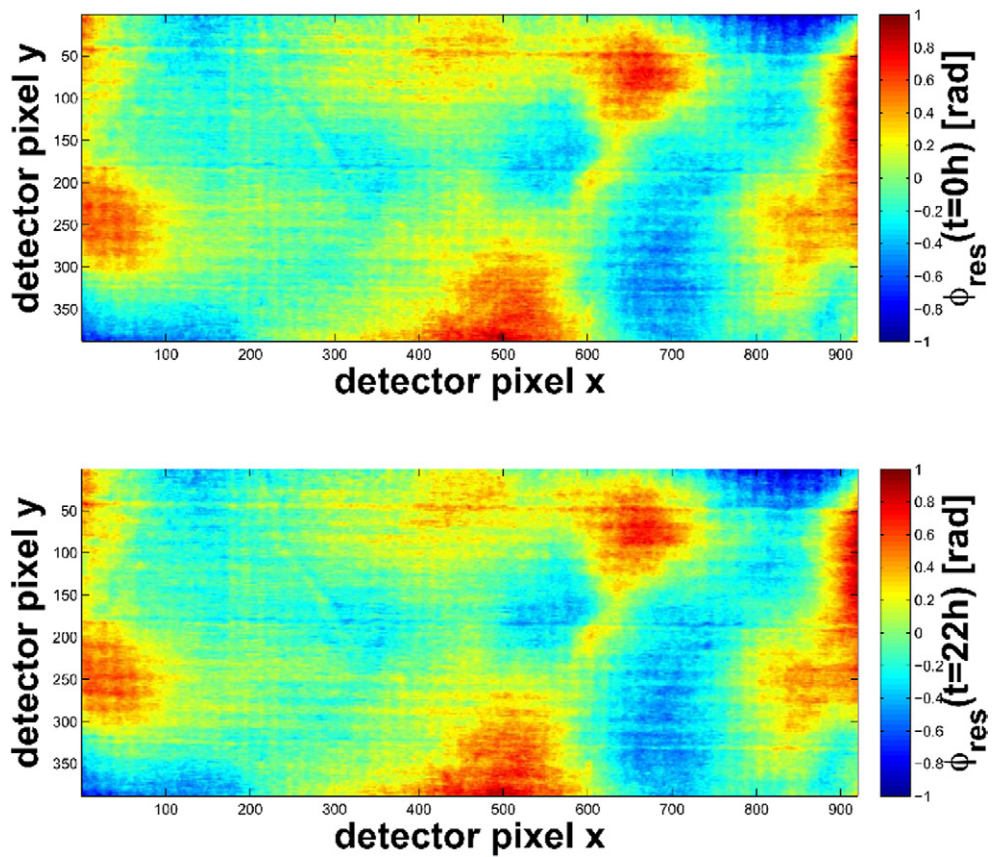
Figure 7. Graphic representation of the residuals $\phi_{res}(x, y, t) = \phi_{unwrap}(x, y, t) - \phi_{fit}(x, y, t)$ taken at the beginning of the measurement ($t = 0$ h) (top) and after 22 h ($t = 22$ h) (bottom).

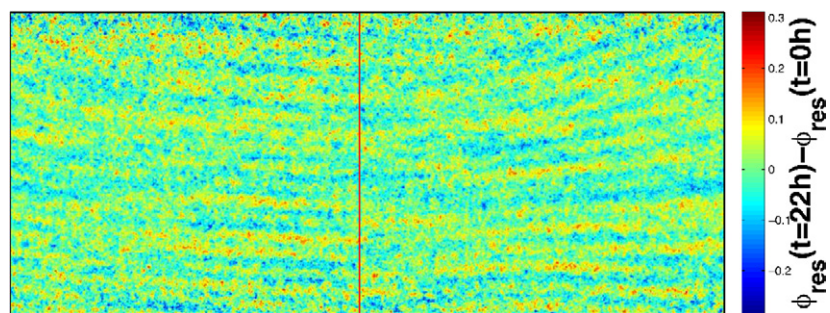**Figure 8.** Difference of the residuals shown in figure 7 which are taken at $t = 0$ h and $t = 22$ h. $\phi_{res}(t = 22$ h$) - \phi_{res}(t = 0$ h$)$. The red line shows the position of the line plot in figure 9.
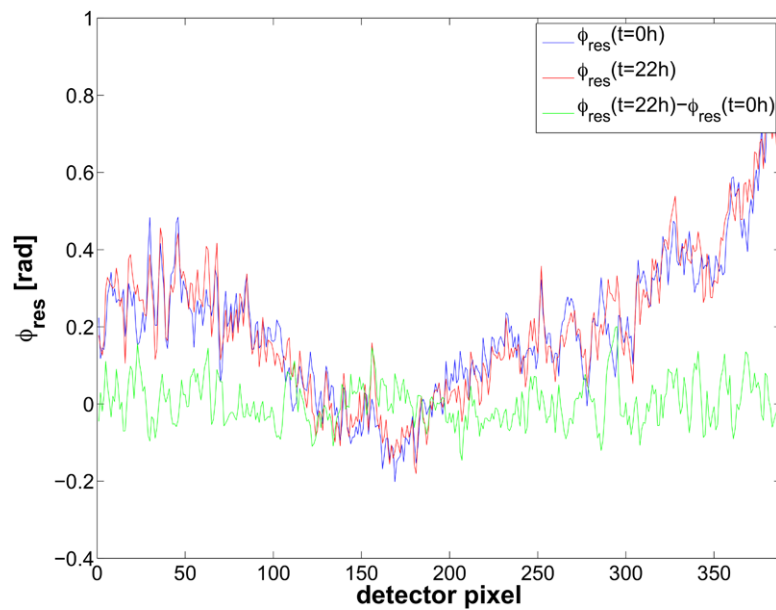
Figure 9. Lineplot of the residuals shown in figure 7 which are taken at $t = 0$ h (blue) and $t = 22$ h (red) and of the difference of these residuals $\phi_{\text{res}}(t = 22 \text{ h}) - \phi_{\text{res}}(t = 0 \text{ h})$ (green).

reproduced. Thus, the PPF method acts like a high-pass filter. Edges in the phase-contrast image are pronounced and will be more easily recognizable.

The whole algorithm has been applied in matlab. Therefore, standard matlab applications have been used.

2.5. Short-term drift effect

To get information about the phase and visibility in each pixel, a phase-stepping is performed. Applying standard reconstruction, a sinusoidal curve is fitted in the measured intensities of each detector pixel. In order to extract the correct phase, amplitude and offset of the sine the phase-step positions $\kappa(n)$ of G2 have to be known precisely. Reconstructing an image using wrong phase-step positions leads to artifacts in the reconstructed image. These artifacts are visible as a Moiré pattern. The Moiré pattern is caused by superposition of two periodical structures (Tavassoly and Samavati 2014). As the phase-step positions are not the same for each image, the superposing periodical structures differ between the images. Thus, the Moiré pattern is not stable and it is not the same in reference and object phase image. For this reason it does not cancel, calculating the differential phase-contrast image. Hence, it is still visible in reconstructed phase images. This can be avoided by the knowledge of the accurate phase-step positions.

In general, it is assumed that all phase-step positions are distributed equidistantly over a predefined number of grating periods. During the imaging process vibrations, distortions and thermal influences on the setup lead to inaccuracies of these phase-step positions. Consequently, the assumption of equidistantly distributed phase-step positions is not valid anymore. Vargas *et al* (2011), (2013) proposed to perform a principal component analysis (PCA) of the measured intensities $I(n)$ in each pixel (x, y) to extract the phase

information from randomly distributed interferograms. Pelzer *et al* (2015) transferred this algorithm to differential phase-contrast imaging in Talbot–Lau interferometry. The following assumptions and calculations are taken from the publication by Vargas *et al* (2011), (2013):

The intensity $I(x, y, n)$ measured at each phase-step $n \in \{1, ..., N\}$ in each detector pixel (x, y) can be described by

$$I(x, y, n) = a(x, y) + b(x, y) \cos(\phi(x, y) + \kappa(n)) \tag{5}$$

where $a(x, y)$ is the background intensity, $b(x, y)$ and $\phi(x, y)$ describe the periodic modulation of the intensity pattern and $\kappa(n)$ describes the phase-step position. Vargas *et al* rewrite this equation as

$$I(x, y, n) = a(x, y) + b(x, y) \left[\cos(\phi(x, y)) \cos(\kappa(n)) - \sin(\phi(x, y)) \sin(\kappa(n)) \right] \tag{6}$$

and group the terms as:

$$I(x, y, n) = a(x, y) + \alpha(n) I_c(x, y) + \beta(n) I_s(x, y) \tag{7}$$

with $\alpha(n) = \cos(\kappa(n))$, $\beta(n) = -\sin(\kappa(n))$, $I_c(x, y) = b \cos(\phi(x, y))$ and $I_s(x, y) = b \sin(\phi(x, y))$. In the following Vargas *et al* subtract the background intensity and assume that $a(x, y) \simeq \frac{1}{N} \sum_{n=1}^{N} a(x, y, n)$ is the mean background intensity over all phase-steps. The PCA is performed with the background filtered intensity

$$I'(x, y, n) = I(x, y, n) - a(x, y) = \alpha(n) I_c(x, y) + \beta(n) I_s(x, y). \tag{8}$$

Therefore, the signal can be expressed as a linear combination of two signals. Vargas *et al* assume that $I_c(x, y)$ and $I_s(x, y)$ are nearly linear independent if there is more than one Moireé fringe in the image. With the help of the PCA a coordinate transformation is performed to find the proper linear independent solution of this problem.

Regarding image reconstruction Vargas *et al* propose to rewrite the matrix $I(x, y, n)$ of size $N_x \times N_y \times N$ into a two dimensional vector $I(z, n)$ of size $N_x \cdot N_y \times N$. The first step of the algorithm requires the covariance matrix C, which is calculated by

$$C(I(z, n), N) = \left(I(z, n) - \frac{1}{N} \sum_{n=1}^{N} I(z, n) \right) \left(I(z, n) - \frac{1}{N} \sum_{n=1}^{N} I(z, n) \right)^T. \tag{9}$$

In a second step, the diagonalisation of C is calculated numerically. Therefore, a singular-value-decomposition algorithm providing the transformation-matrix A is used.

$$
\begin{aligned}
D &= ACA^T \\
&= A \left(I(z, n) - \frac{1}{N} \sum_{n=1}^{N} I(z, n) \right) \left(I(z, n) - \frac{1}{N} \sum_{n=1}^{N} I(z, n) \right)^T A^T \\
&= YY^T
\end{aligned} \tag{10}
$$

The transformation matrix A rotates the measured intensity vectors in a new coordinate system with orthogonal axes, the principal components Y_i (with $i \in \{1, ..., \text{number of principal components}\}$).

We calculated the principal component analysis using a standard application in matlab.

Vargas *et al* (2013) also propose a possibility to calculate the phase-step positions from the principal components Y. It is assumed that, after reshaping the vector of intensities $I(n)$ and the vector of principal components Y to matrices $I(x, y, n)$ and $Y_i(x, y)$ of size $N_x \times N_y \times N$ and $N_x \times N_y$, new factors for linear combination can be calculated as follows

$$\alpha^*(x, y, n) = \langle I(x, y, n), Y_1(x, y) \rangle = \sum_{x=1}^{N_x} \sum_{y=1}^{N_y} Y_1(x, y) I(x, y, n) \tag{11}$$

and

$$\beta^*(x, y, n) = \langle I(x, y, n), Y_2(x, y) \rangle = \sum_{x=1}^{N_x} \sum_{y=1}^{N_y} Y_2(x, y) I(x, y, n). \tag{12}$$

$Y_1(x, y)$ and $Y_2(x, y)$ are the first two principal components of $Y_t(x, y)$. Using equations (11) and (12) the optimized and denoised intensity without the background intensity can be calculated as

$$I'^*(x, y, n) = \alpha^*(x, y, n) Y_1(x, y) + \beta^*(x, y, n) Y_2(x, y). \tag{13}$$

As it was defined that $\alpha(n) = \cos(\kappa(n))$, $\beta(n) = -\sin(\kappa(n))$, the new, optimized phase-step positions can be calculated with

$$\kappa^*(n) = \tan^{-1}\left(\frac{-\beta^*(n)}{\alpha * (n)}\right). \tag{14}$$

Vargas *et al* further optimize the phase-step positions by a least square minimization. In a first step, they assume that for each phase-step position the new, optimized intensity $I'^*(x, y, n)$ should be the same as the measured intensity $I'(x, y, n)$. Calculating the difference between measured and calculated intensity Vargas *et al* also consider the DC-term $a^*(x, y)$.

$$S(x, y) = \sum_{n=1}^{N} (a^*(x, y) + I'^*(x, y, n) - I'(x, y, n))^2$$
$$= \sum_{n=1}^{N} (a^*(x, y) + \alpha^*(n) Y_1(x, y) + \beta^*(n) Y_2(x, y) - I'(x, y, n))^2 \tag{15}$$

The least square minimization is performed by assuming that

$$\frac{\partial S(x, y)}{\partial a^*(x, y)} = 0, \qquad \frac{\partial S(x, y)}{\partial Y_1(x, y)} = 0, \qquad \frac{\partial S(x, y)}{\partial Y_2(x, y)} = 0. \tag{16}$$

Performing the minimization algorithm $Y_1(x, y)$ and $Y_2(x, y)$ can be optimized. With the help of these optimized principal components Vargas *et al* also assume that the measured intensity $I'(x, y, n)$ in each pixel (x, y) should be the same as the the optimized intensity $I'^*(x, y, n)$. A second least square minimization is performed to optimize $\alpha^*(n)$ and $\beta^*(n)$.

$$S(n) = \sum_{i=1}^{N_x \times N_y} (a^*(n) + I'^*(x, y, n) - I'(x, y, n))^2$$
$$= \sum_{i=1}^{N_x \times N_y} (a^*(n) + \alpha^*(n) Y_1(x, y) + \beta^*(n) Y_2(x, y) - I'(x, y, n))^2 \tag{17}$$

with

$$\frac{\partial S(n)}{\partial a^*(n)} = 0, \qquad \frac{\partial S(n)}{\partial \alpha^*(n)} = 0, \qquad \frac{\partial S(n)}{\partial \beta^*(n)} = 0. \tag{18}$$

As $\alpha^*(n)$ and $\beta^*(n)$ are improved by this method new $\kappa^*(n)$ can be calculated. These two minimization algorithms are performed iteratively until the phase-step positions $\kappa_k^*(n)$ converge (with $k \in \{1, .., \text{maximal number of iterations}\}$). The convergence criterion of Vargas *et al* is announced as

$$\max_n |\kappa_k^*(n) - \kappa_{k-1}^*(n)| < \epsilon. \tag{19}$$

with $\epsilon = 10^{-2}$ rad.

Henceforth, we use the described algorithm of Vargas *et al* to reduce artifacts in the image modalities. For further reconstruction of phase, amplitude and offset the sinusoidal-fit is performed.

The whole algorithm has been written in matlab code to reconstruct the following images.

Calculating the principal components the order of the first two principal components Y_1 and Y_2 is random. Both components have the same weight calculating the signal as they represent the sine and the cosine component of the signal. This results in random phase-shift offsets of π between the single reconstructions of the phase image. As large objects are imaged with the help of a tiling-procedure it might happen that adjacent tiles of the phase-contrast image have different signs or even that the sign of the phase of the reference image differ from the sign of the phase of the object image. To reconstruct the phase-contrast image the residuals of one reference phase $\phi_{\mathrm{res, ref}}$, as described in the paragraph section 2.4, can be used. As these residuals are independent in time they should be the same in each tile of the reference measurement. Hence, the residuals $\phi_{\mathrm{res, ref(m)}}$ (with $m \in \{1, ..., \text{number of reference images}\}$) of each reference tile are calculated and compared to the residuals of a first reference tile $\phi_{\mathrm{res, ref(1)}}$ by calculating the standard deviation over all pixel in the FoV of $\sigma^- = \mathrm{std}(\phi_{\mathrm{res, ref(m)}} - \phi_{\mathrm{res, ref(1)}})$ and $\sigma^+ = \mathrm{std}(\phi_{\mathrm{res, ref(m)}} + \phi_{\mathrm{res, ref(1)}})$. If $\sigma^+ < \sigma^-$ holds true, $\phi_{\mathrm{ref(m)}}$ is multiplied by -1.

The analogue approach is used to examine the sign between object- and reference-phase. The standard deviation of $\sigma^-_{\Delta\phi} = \mathrm{std}(\phi_{\mathrm{obj(n)}} - \phi_{\mathrm{ref(n)}})$ and $\sigma^+_{\Delta\phi} = \mathrm{std}(\phi_{\mathrm{obj(n)}} + \Phi_{\mathrm{ref(n)}})$ are calculated. If $\sigma^+_{\Delta\phi} < \sigma^-_{\Delta\phi}$ holds true, $\phi_{\mathrm{obj(n)}}$ is multiplied by -1.

3. Results

3.1. Long-term drift effects

To visualize and compare the results of the different reconstruction techniques the image of a human hand consisting out of 70 tiles is taken. The PPF method was carried out to reconstruct the image with just one reference image. Without this reconstruction algorithm it is necessary to move the object repeatedly out of the beam during the measurement to take a reference image. In case of the presented measurement ten reference images were taken. The phase-contrast image of the human hand reconstructed using just one reference image is shown in figure 3. In this case object information is superimposed by phase drifting effects. Figure 10 (bottom) shows the reconstruction of the same data set with the help of the PPF algorithm by using just one reference image. For the differential phase-contrast image shown in figure 10 on the top the reference image has been always renewed after taking one row of (seven) object tiles. Hence, ten reference images were taken during the measurement. To investigate the difference between the results of both reconstruction algorithms, the quotient between the image reconstructed using the PPF method and the image reconstructed using the standard sine fit method and ten reference images is calculated, which can be seen in figure 11. Dividing both images, structures which are the same in both images cancel out. Thus, only structures which are different in the images are preserved in figure 11. It can be observed that tiny structures like the bones in the metacarpus cancel out, dividing both reconstruction modalities as they are represented in both images. However, hard edges are still visible after dividing the images. This is due to the high-pass behaviour of the PPF method. Large spacial frequency properties of the object are not represented in the image reconstructed using the PPF algorithm. Therefore, hard edges are pronounced using the PPF algorithm. This can be seen, comparing the images in figure 10.
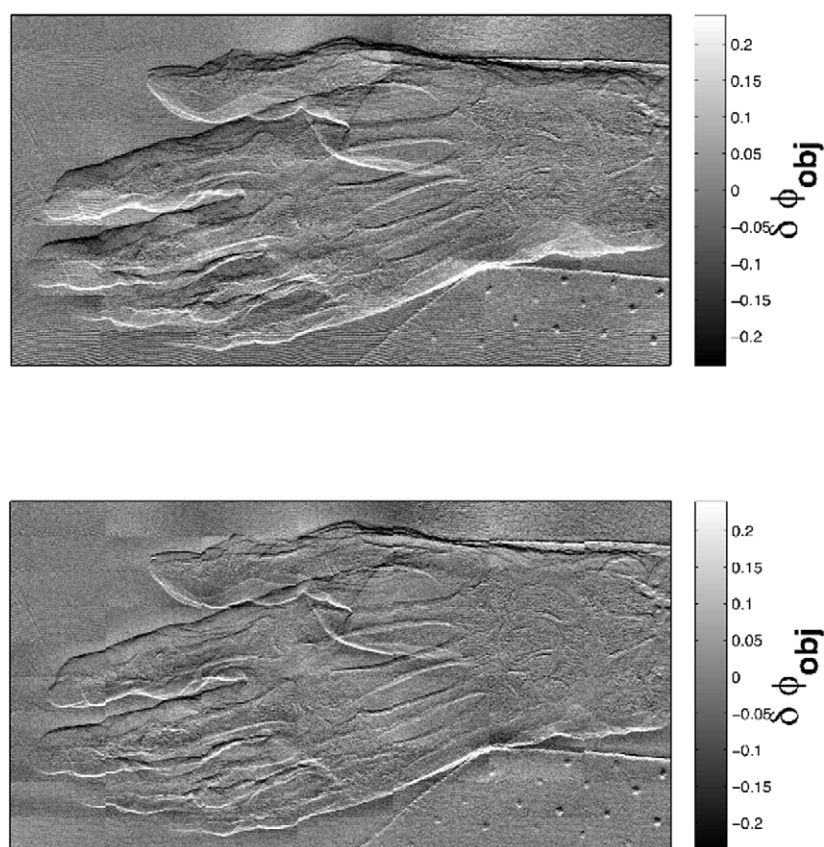
Figure 10. Differential phase-contrast image of a human hand reconstructed with the sine fit method and 10 reference measurements (top). Differential phase-contrast image reconstructed with the help of the PPF algorithm (bottom). Just one reference measurement is necessary to reconstruct this image. For both images the same windowing parameters are chosen $[-0.25\,\text{rad}, 0.25\,\text{rad}]$.

To analyse the Moiré pattern in the images of figure 10, which appear as an indicator for the image quality, a fast-Fourier-transformation is performed (figure 12). The diagram on top of figure 12 shows the frequencies of the image reconstructed with the conventional sine-fitting algorithm. The diagram on the bottom of figure 12 shows the frequencies represented in the image which is reconstructed using the PPF algorithm. In both images the two peaks next to the central peak around the y-frequency of about $1500\,\frac{1}{\text{pixel}}$ and $-1500\,\frac{1}{\text{pixel}}$ can be identified as the frequencies of the Moiré pattern. It can be seen that the peaks caused by the frequencies of the Moiré pattern, are less dominant in the PPF reconstructed images as in the frequency spectrum of the conventional reconstructed image. This is due to the fact that the Moiré pattern of the reference phase influences the differential phase image. The only components causing a Moiré pattern using the PPF reconstruction algorithm are the Moiré pattern of the object phase and the Moiré pattern of the residuals. Thus, there are less components which cause an amplification of the Moiré pattern. Instead, the PPF algorithm produces different, smaller frequency peaks. A grid-like pattern can be observed, in the FFT of the image calculated with the PPF method. This pattern can be explained by slight vibrations
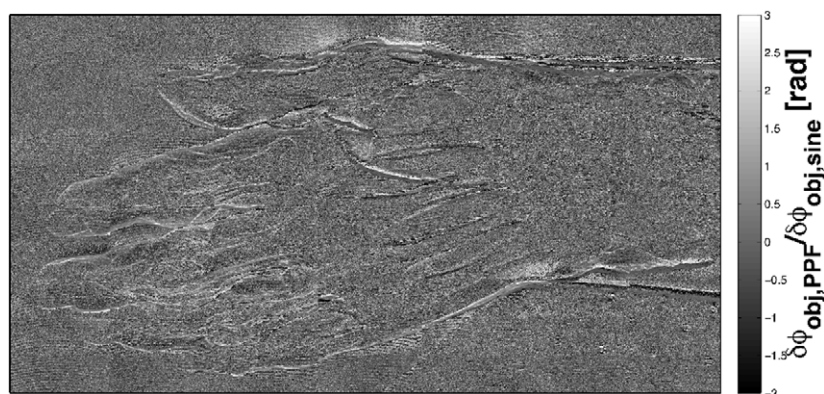
Figure 11. Differential phase-contrast image reconstructed with the help of the PPF algorithm (figure 10, bottom) divided by differential phase-contrast image of a human hand reconstructed with the sine fit method and 10 reference measurements (figure 10, top).

of the setup which causes vibrations of the residuals. As the residuals are caused inter alia by artifacts of the gratings, vibrations of these residuals lead to periodic, grid-like artifacts in the FFT image. These vibrations have been neglected in the PPF algorithm. The resulting artifacts might mainly be observed as noise in the images. With the help of a gauss filter the artifacts can be reduced as they are of high frequency. Such kind of image cleaning is not considered in this paper. Even in the FFT of the conventional reconstructed image the artifacts of the gratings can be seen as slight, vertical lines. These slight lines can be explained by imprecise phase-step positions as they can be reduced by applying the PCA minimization algorithm (see section 3.2).

3.2. Short-term drift effects

To analyze the effects of the PCA minimization algorithm the single phase-step positions are examined. As acquisition parameters have been chosen eleven phase-steps, equidistantly distributed over two periods (4π). As the PCA algorithm arranges the phase-steps over 2π (figure 15) an unwrapping algorithm has been performed for better comparability of the two distributions (figure 16). The phase-step positions reconstructed by applying the PCA minimization algorithm are not equidistantly distributed as it is shown in figure 13. To clarify the derivations a line fit has been performed. The red dots are not distributed on a straight line over the phase-step numbers. For example phase-step number 9 is not in line with phase-steps number 8 and 10. Furthermore, instead of increasing phase-step positions the phase-step positions decrease after applying the PCA-minimization algorithm. The different stepping directions only affect the phase of the measured phase-stepping curves. They will be displaced relative to each other by 2π. The amplitude and the mean value of the curve do not change because of this shift. Hence, there is no effect on dark-field and attenuation images. The effect on the phase is caused by interchanging the first two principal components Y_1 und Y_2. How to handle the phase-shift of π is described in the section 2.5. The offset between the two curves in figure 14 is caused by the definition of the zero point. In the standard reconstruction the first phase-step position is set as zero point. In PCA reconstruction the zero point is set randomly. As the choice of the zero point is the same for all pixel for one reconstruction method and just the differences between the values of each pixel are important, the choice of the zero point does not affect the resulting image.
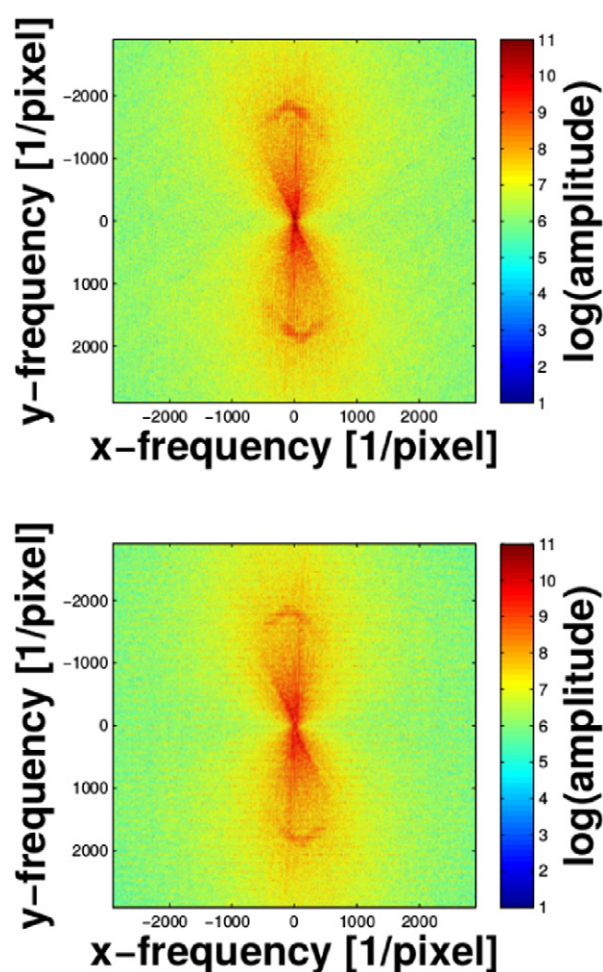
Figure 12. 2D FFT of the differential phase-contrast images of figure 10. Reconstruction with the help of the conventional sine-fitting reconstruction, with ten reference images used (top), PPF algorithm, with only one reference image used (bottom).

For the sake of better comparability of the phase-step positions, in figure 14 the phase-step directions of the two curves are adapted to each other by multiplying the PCA-phase-steps by -1. Again an unwrapping of the phase-step positions calculated using the PCA algorithm has been performed. By default the phase-stepping grating G_2 should have been moved by $\frac{4\pi}{11}$. It is obvious that after performing the PCA-minimization algorithm it is assumed that the grating does not move equidistant steps. The moved distances are sometimes smaller and sometimes larger than the predefined $\frac{4\pi}{11}$. These differences can be explained either by an imperfect positioning of the G_2 positioning system (blue positions) or by an imperfect reconstruction of the PCA method (red positions). By calculating the χ^2 of the sine-fit in both phase-step positions, it can be observed that the mean of χ^2 is always smaller for the PCA reconstructed phase-step positions than for the equidistantly distributed phase-step positions. For the ten reference images the following χ^2 values (in arbitrary units) can be calculated:
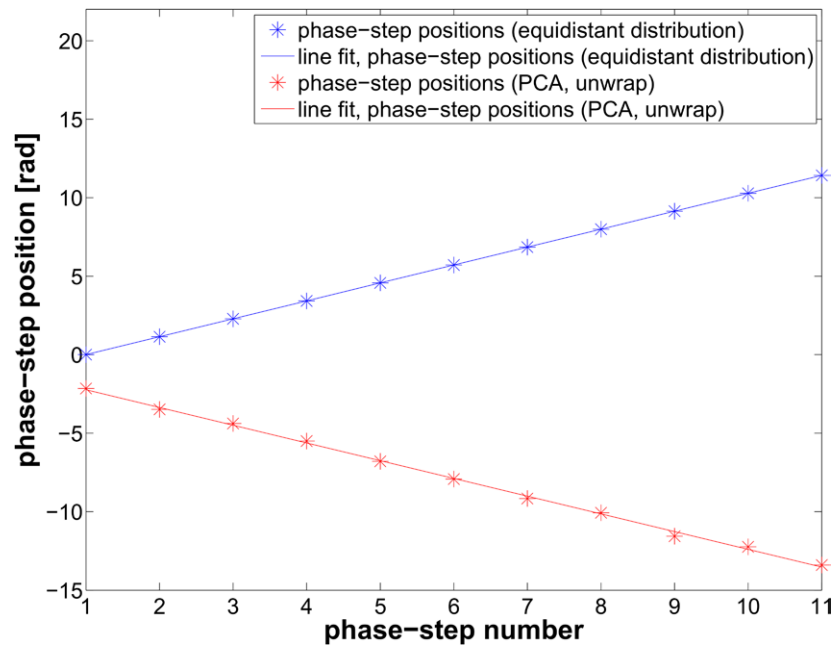
Figure 13. Phase-step positions as function of the number of phase-steps. Predefined phase-step positions over 4π (blue), reconstructed phase-step positions from the PCA minimization algorithm (red). A line fit has been performed to illustrate the derivation of an equidistant distribution of the phase-steps after applying the PCA algorithm.

$\langle \chi^2_{\text{ref, PCA}} \rangle = 5.8 \pm 3.1$ and $\langle \chi^2_{\text{ref, equi.dist.}} \rangle = 11.7 \pm 5.7$. For the 70 object tiles the χ^2 (in arbitrary units) is: $\langle \chi^2_{\text{obj, PCA}} \rangle = 5.5 \pm 3.1$ and $\langle \chi^2_{\text{obj, equi.dist.}} \rangle = 6.5 \pm 3.5$. Thus, the mean quality of the fit is better for the PCA reconstructed phase-step positions than for the assumed equidistant phase-step positions.

In figure 15 it can be seen that the curve of the detector intensities over the phase-step positions is shifted by applying the PCA minimization algorithm. This is due to the different choice of the zero points. Using the PCA all curves are shifted the same compared to the standard reconstruction. Thus the shift is not visible in the resulting differential phase-contrast image.

Figure 17 shows comparisons between the conventional sine-fitting reconstruction and the PCA minimization reconstruction for all three imaging modalities. To be able to show more detail, the figures show a crop depicting the metacarpus of a human hand. Figures 17(A), (C) and (E) show the images reconstructed using the sine-fitting algorithm, figures 17(B), (D) and (F) the images reconstructed using the PCA minimization algorithm. The attenuation images do not differ between both reconstruction techniques. The offset of the fitted sine is obviously not heavily dependent on the different phase-step positions. But in the differential phase-contrast image and in the dark-field image the Moiré pattern can be nearly completely removed. Just one tile on the top right corner in the dark-field image (figure 17(F)) still shows the Moiré pattern. This is caused by the reason the Moiré pattern arises. In the other tiles the Moiré pattern is due to the assumption of false phase-step positions. This can be corrected by applying the PCA minimization algorithm. The Moiré pattern in the tile on the top right corner is caused by very short-term effects. The setup has not been stable during the acquisition of one phase-step. This effect cannot be removed by the PCA minimization algorithm. But for all other tiles the image quality can be improved by applying the PCA minimization algorithm.
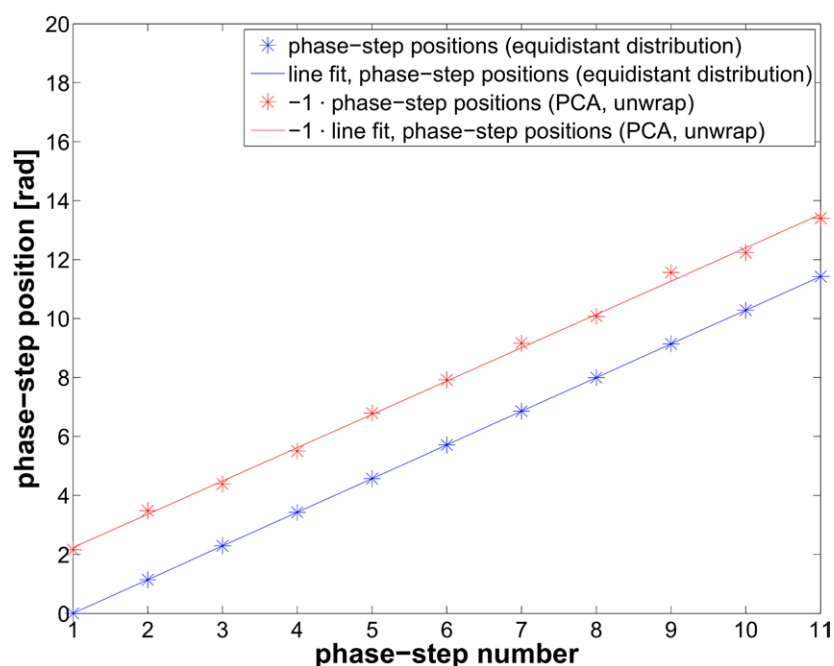
Figure 14. Phase-step positions as function of the number of phase-steps. Predefined phase-step positions over 4π (blue), reconstructed phase-step positions from the PCA minimization algorithm (red). For better comparability the phase-step positions calculated using the PCA algorithm have been multiplied by -1. A line fit has been performed to illustrate the derivation of an equidistant distribution of the phase-steps after applying the PCA algorithm.

To analyse the Moiré pattern in the images of figure 17 a fast-Fourier-transformation of all images is performed (figure 18). The plots on top of figures 18(A), (C) and (E) show the frequencies of the three imaging modalities reconstructed with the conventional sine-fitting algorithm. The two peaks next to the central peak of the differential phase-contrast image and of the dark-field image around the y-frequency of about $1500 \frac{1}{\text{pixel}}$ and $-1500 \frac{1}{\text{pixel}}$ can be identified as the frequencies of the Moiré pattern. The plots on the bottom of figures 18(B), (D) and (F) show the frequencies represented in the images which are reconstructed with the help of the PCA minimization algorithm. Regarding the frequency spectra of the attenuation images, both images are completely the same. Thus, the PCA minimization algorithm does not affect the attenuation image and the information of the attenuation image is preserved. Furthermore, it can be seen that the frequency spectra of the differential phase-contrast images only differ considering the frequency peaks caused by the Moiré pattern. These peaks can be reduced by using the PCA without modifying the rest of the frequency spectrum. In the frequency spectrum of the conventionally reconstructed image slight vertical lines can be observed. These lines can be explained by grating inhomogeneities as they are perpendicular to the grating bars. Due to the inaccurate phase-step positions, the positions of the inhomogeneities differ between the reference measurement and the measurement with the object in the beam-path. The resulting artifacts can be observed as lines in the frequency spectrum. Applying the PCA minimization algorithm these artifacts can be reduced as the phase-step positions are adjusted. Thus, the lines are less visible in the frequency spectrum of the image reconstructed using
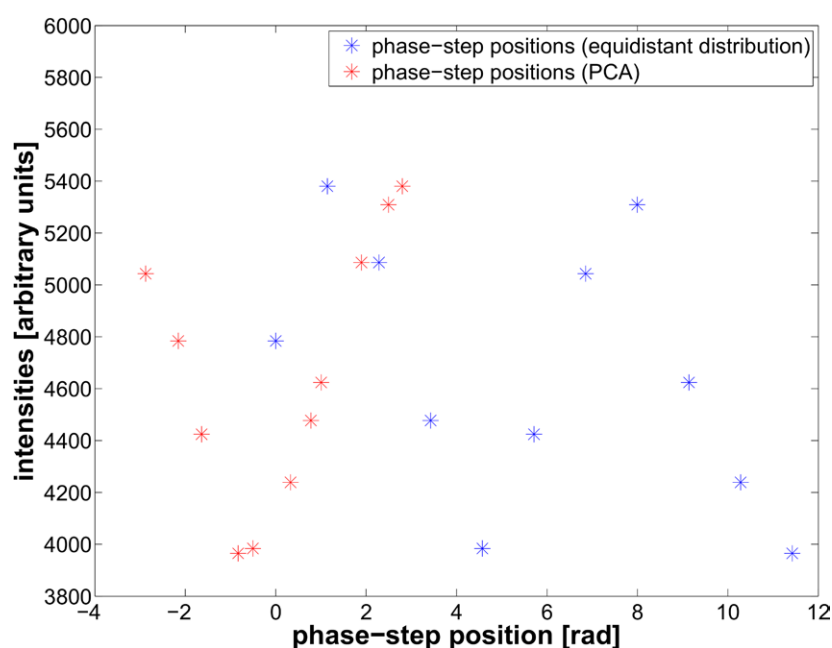
Figure 15. Measured intensity in arbitrary units in one pixel of the detector matrix of a reference measurement as function of the phase-step position. Predefined phase-step positions over 4π (blue), reconstructed phase-step positions from the PCA minimization algorithm (red).

the PCA minimization algorithm. Even in the frequency spectrum of the dark-field image reconstructed with the help of the PCA minimization algorithm, the peaks of the Moiré pattern are almost removed. Like for the differential phase-contrast image the rest of the frequency spectrum is not affected by the PCA minimization algorithm.

4. Discussion

4.1. Long-term drift effects

It can be shown that it is possible to reconstruct an useful and meaningful image based on just one reference image. Relevant anatomic structures are visible (figures 10 and 11). The frequency spectra of the conventional sine-fitting reconstruction method and of the PPF method only differ concerning the Moiré frequency peaks. These can be reduced in amplitude by performing the PPF method. Thus, the image artifacts caused by the Moiré pattern can be slightly reduced by performing the PPF algorithm without further image processing (figure 12).

Slight artifacts occur because of the vibration of the residuals due to the vibration of the setup. This causes additional noise in the images. The additional noise does not lower the image quality as much as all structures are still visible and the frequency spectra are nearly similar.

The PPF methods has the advantage that instead of moving the object several times out of the setup, just one reference image is needed for a whole of 70 tiles. As an advantage, the object movement is minimized as it stays inside the setup during the whole time of the measurement. For a clinical workflow a reference image would be needed once per several hours only.
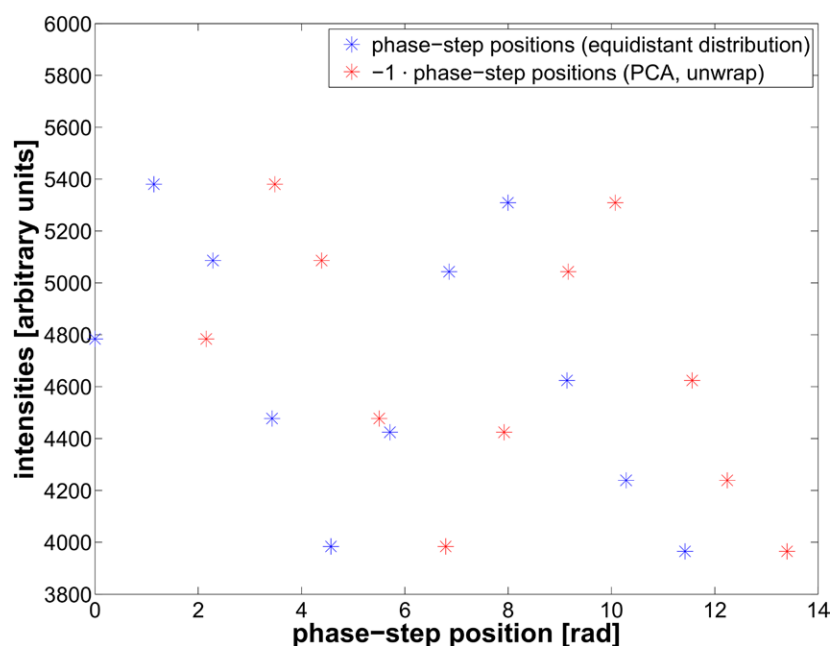
Figure 16. Measured intensity in arbitrary units in one pixel of the detector matrix of a reference measurement as function of the phase-step position. Predefined phase-step positions over 4π (blue), reconstructed phase-step positions from the PCA minimization algorithm (red). For better comparability the phase-step positions calculated using the PCA algorithm have been unwrapped and multiplied by -1.
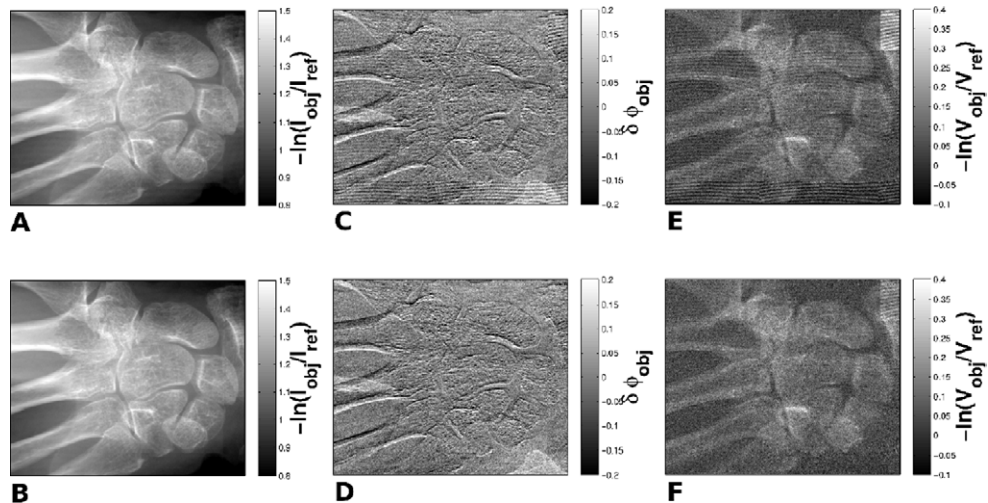

Figure 17. (A) and (B): attenuation images of the metacarpus of a human hand. (C) and (D): differential phase-contrast images of the metacarpus of a human hand. (E) and (F): dark-field images of the metacarpus of a human hand. Reconstruction with the help of the conventional sine-fitting reconstruction (top, (A), (C) and (E)), PCA minimization algorithm (bottom, (B), (D) and (F)). For all image reconstructions ten reference images are taken. Thus, the reference image has been always renewed after seven object tiles.
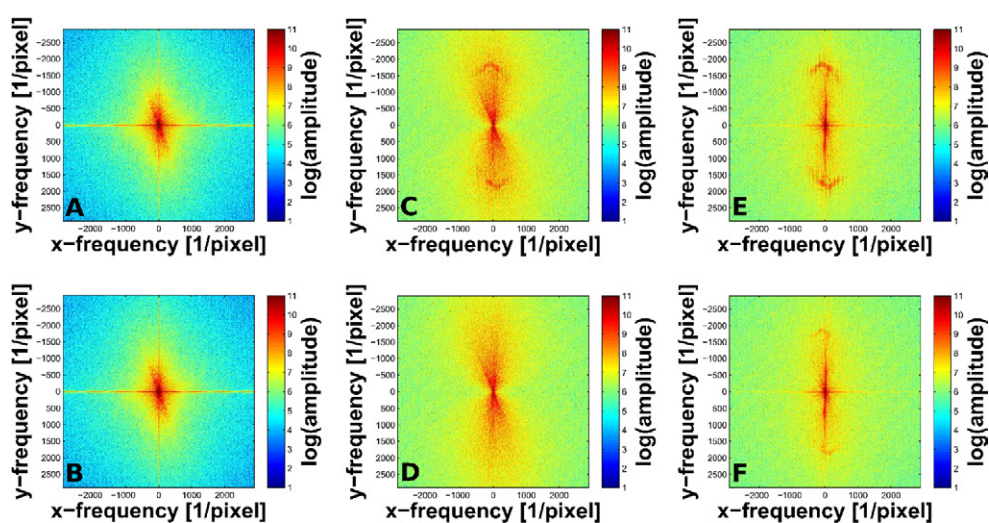
Figure 18. 2D FFT of the images of figure 17. (A) and (B): 2D FFT of the attenuation images. (C) and (D): 2D FFT of the differential phase-contrast images. (E) and (F): 2D FFT of the dark-field images. Reconstruction with the help of the conventional sine-fitting reconstruction (top, (A), (C) and (E)), PCA minimization algorithm (bottom, (B), (D) and (F)).

4.2. Short-term drift effects

Reconstructing images with the help of the PCA algorithm of Vargas *et al* does not need the knowledge of the phase-step positions. As in clinical and other setups, which are integrated in work processes, it cannot be ensured that the setup is stable like on an optical stage, this is an important feature regarding the integration of phase-contrast imaging in work processes. Errors in the presumed phase-step positions caused by vibrations and distortions of the setup can be corrected with the help of the PCA minimization algorithm. Figure 17 shows that the Moiré pattern is reduced by applying the PCA minimzation algorithm. The related artifacts in differential phase-contrast images and dark-field images can be reduced or even removed. Especially in dark-field images this has a great impact on image quality. With the help of the PCA it is possible to reconstruct the three images of Talbot–Lau interferometry. In figure 18 the frequency spectra of the three images, reconstructed with the help of the PCA minimization algorithm of Vargas *et al* and reconstructed with the help of the conventional sine-fitting algorithm are shown. It can be seen that the frequency of the Moiré pattern can be almost removed in the differential phase-contrast image and in the dark-field image by applying the PCA minimization algorithm. The rest of the frequency spectrum is not affected by the PCA minimization algorithm. Thus, the imaged information is the same for both reconstruction techniques and just the image artifacts are removed.

5. Conclusion

We were able to show that it is possible to handle several drifting effects which occur when transferring a phase-contrast imaging system to a conventional medical setup. Imaging artifacts caused by short term drifting effects and mechanical inaccuracies can be removed by applying the algorithm proposed by Vargas *et al*. It can be shown that frequencies of the Moiré pattern can be reduced or even removed. Additionally, it is possible to shorten imaging

time without lowering the image quality. This will be interesting features with regard to the implementation of this imaging method in non-destructive testing and clinical processes. Tiny lesions can be detected with lower dose exposure and in less time than has been the case so far as it is not necessary any more to take the mean of several images to reduce artifacts. As it is possible to reconstruct images without knowing the phase-step positions and only one reference image, fluoroscopy, life-time imaging might be possible. This is an important feature with regard to clinical applications.

6. Outlook

For further examinations of the PPF method it would be interesting to quantify the exact time-span for which the so called residuals are stable. That means that it should be investigated how often the calibration image should be renewed. Therefore, different external parameters could be changed and the validity of the residuals under these different impacts could be examined.

Prospectively, with larger gratings the acquisition time for differential phase-contrast imaging will go down to the acquisition time of conventional x-ray imaging. Thus, the whole process will be feasible even for imaging living objects like humans or animals.

Furthermore, the feasibility of the PCA minimization algorithm for fluoroscopy should be tested.

In the future, it is an interesting aspect to try to apply the PPF method and PCA minimization algorithm for differential phase-contrast CT reconstruction. During CT acquisition it is not possible to renew the reference image. Additionally, the CT setup might not be mechanical stable during the whole acquisition procedure.

Thus, both presented algorithms will improve the feasibility of x-ray Talbot–Lau imaging for conventional workflow.

Acknowledgment

References

Bartelt H and Jahns J 1979 Interferometry based on the Lau effect *Opt. Commun.* **30** 268–74
Bech M, Tapfer A, Velroyen A, Yaroshenko B, Pauwels B, Hostens J, Bruyndonckx P, Sasov A and Pfeiffer F 2013 *In vivo* dark-field and phase-contrast x-ray imaging *Sci. Rep.* **3** 3209
Bravin A 2003 Exploiting the x-ray refraction contrastwith an analyser: the state of the art *J. Phys. D: Appl. Phys.* **36** A24–9
Chapman D, Thomlinson W, Johnston R, Washburn D, Pisano E, Gmuer N, Zhong Z, Menk R, Arfelli F and Sayers D 1997 Diffraction enhanced x-ray imaging *Phys. Med. Biol.* **42** 2015–25
Clauser J and Reinsch M 1992 New theoretical and experimental results in Fresnel optics with applications to matter-wave and x-ray interferometry *Appl. Phys.* B **54** 380–95
David C, Noehammer B, Solak H and Ziegler E 2002 Differential x-ray phase contrast imaging using a shearing interferometer *Appl. Phys. Lett.* **81** 3287–9
David C, Pfeiffer F and Weitkamp T 2006 Interferometer for quantitative phase contrast imaging and tomography with an incoherent polychromatic x-ray source *European Patent* application no. EP05012121

Diemoz P, Bravin A and Coan P 2012 Theoretical comparison of three x-ray phase-contrast imaging techniques: propagation-based imaging, analyzer-based imaging and grating interferometry *Opt. Express* **20** 2789–805

Engelhardt M, Kottler C, Bunk O, David C, Schroer C, Baumann J, Schuster M and Pfeiffer F 2008 The fractional talbot effect in differential x-ray phase-contrast imaging for extended and polychromatic x-ray sources *J. Microsc.* **232** 145–57

Fitzgerald R 2000 Phase-sensitive x-ray imaging *Phys. Today* **53** 23–6

Foerster E, Goetz K and Zaumseil P 1980 Double crystal diffractometry for the characterization of targets for laser fusion experiments *Krist. Technol.* **15** 937–45

Jahns J and Lohmann A 1979 The Lau effect (a diffraction experiment with incoherent illumination) *Opt. Commun.* **28** 263–7

Koehler T, Daerr H, Martens G, Kuhn N, Löscher S, van Stevendaal U and Roessl E 2015 Slit-scanning differential x-ray phase-contrast mammography: proof-of-concept experimental studies *Med. Phys.* **42** 1959

Lau E 1948 Beugungserscheinungen an doppelrastern *Ann. Phys.* **437** 417–23

Li K, Ge Y, Garrett J, Bevins N, Zambelli J and Chen G-H 2014 Grating-based phase contrast tomosynthesis imaging: proof-of-concept experimental studies *Med. Phys.* **41** 011903

Lohmann A and Silva D 1971 An interferometer based on the talbot effect *Opt. Commun.* **2** 413–5

Michel T *et al* 2013 On a dark-field signal generated by micrometer-sized calcifications in phase-contrast mammography *Phys. Med. Biol.* **58** 2713–32

Momose A, Kawamoto S, Koyama I, Hamaishi Y, Takai K and Suzuki Y 2003 Demonstration of x-ray talbot interferometry *Japan. J. Appl. Phys.* **52** L866–8

Momose A, Takeda T, Itai Y and Hirano K 1996 Phase-contrast x-ray computed tomography for observing biological soft tissues *Nat. Med.* **2** 473–5

Olivo A *et al* 2001 An innovative digital imaging set-up allowing a low-dose approach to phase contrast applications in the medical field *Med. Phys.* **28** 1610–9

Olivo A, Ignatyev K, Munro P R T and Speller R D 2011 Noninterferometric phase-contrast images obtained with incoherent x-ray sources *Appl. Opt.* **50** 1765–9

Olivo A and Speller R 2007 A coded-aperture technique allowing x-ray phase contrast imaging with conventional sources *Appl. Phys. Lett.* **91** 1–3

Patorski K 1983 Incoherent superposition of multiple self-imaging Lau effect and Moiré fringe explanation *Opt. Acta: Int. J. Opt.* **30** 745–58

Pelzer G, Rieger J, Hauke C, Horn F, Michel T, Seifert M and Anton G 2015 Reconstruction method for grating-based x-ray phase-contrast images without knowledge of the grating positions *J. Instrum.* **10** P12017

Pfeiffer F, Weitkamp T, Bunk O and David C 2006a Phase retrieval and differential phase-contrast imaging with low-brilliance x-ray sources *Nat. Phys.* **2** 258–61

Pfeiffer F, Weitkamp T and David C 2006b X-ray phase contrast imaging using a grating interferometer *Europhys. News* **37** 13–5

Snigirev A, Snigireva I, Kohn V, Kuznetsov S and Schelokov I 1995 On the possibilities of x-ray phase contrast microimaging by coherent high-energy synchrotron radiation *Rev. Sci. Instrum.* **66** 5486–92

Stampanoni M, Wang Z, Thüring T, David C, Roessl E, Trippel M, Kubik-Huch R A, Singer G, Hohl M K and Hauser N 2011 The first analysis and clinical evaluation of native breast tissue using differential phase-contrast mammography *Investigative Radiol.* **46** 801–6

Suleski T J 1997 Generation of Lohmann images from binary-phase talbot array illuminators *Appl. Opt.* **36** 4686–91

Talbot H 1836 Facts relating to optical science *Philos. Mag. J. Sci.* **9** 401–7

Tapfer A *et al* 2012 Experimental results from a preclinical x-ray phase-contrast CT scanner *Proc. Natl. Acad. Sci.* **109** 15691–6

Tavassoly M T and Samavati K 2014 Formulation of the Moiré fringes formed by superimposing linear gratings with slowly varying parameters *Appl. Opt.* **53** 6612–8

Vargas J, Quiroga J A and Belenguer T 2011 Analysis of the principal component algorithm in phase-shifting interferometry *Opt. Lett.* **36** 2215–7

Vargas J, Sorzano C, Estrada J and Carazo J 2013 Generalization of the principal component analysis algorithm for interferometry *Opt. Commun.* **286** 130–4

Weber T, Bartl P, Bayer F, Durst J, Haas W, Michel T, Ritter A and Anton G 2011 Noise in x-ray grating-based phase-contrast imaging *Med. Phys.* **38** 4133–40

Weitkamp T, David C, Kottler C, Bunk O and Pfeiffer F 2006 Tomography with grating interferometers at low-brilliance sources *Proc. SPIE* **6318** 63180S

Weitkamp T, Diaz A, David C, Pfeiffer F, Stampanoni M, Cloetens P and Ziegler E 2005 X-ray phase imaging with a grating interferometer *Opt. Express* **13** 6296–304

Wilkins S, Gureyev T, Gao D, Pogany A and Stevenson A 1996 Phase-contrast imaging using polychromatic hard x-rays *Nature* **384** 335–8